Use of Synchrotron Radiation-Analytical Techniques To Reveal Chemical Origin of Silver-Nanoparticle Cytotoxicity

Liming Wang,[†,§] Tianlu Zhang,[†,§] Panyun Li,[‡,§] Wanxia Huang,[‡] Jinglong Tang,[†] Pengyang Wang,[†] Jing Liu,[†] Qingxi Yuan,[‡] Ru Bai,[†] Bai Li,[†] Kai Zhang,[‡] Yuliang Zhao,[†] and Chunying Chen*[,†]

[†]CAS Key Laboratory for Biomedical Effects of Nanomaterials and Nanosafety, National Center for Nanoscience and Technology of China and Institute of High Energy Physics, Chinese Academy of Sciences, Beijing, China and [‡]Beijing Synchrotron Radiation Facility, Institute of High Energy Physics, Chinese Academy of Sciences, Beijing, China. [§]These authors contributed equally.

ABSTRACT To predict potential medical value or toxicity of nanoparticles (NPs), it is necessary to understand the chemical transformation during intracellular processes of NPs. However, it is a grand challenge to capture a high-resolution image of metallic NPs in a single cell and the chemical information on intracellular NPs. Here, by integrating synchrotron radiation-beam transmission X-ray microscopy (SR-TXM) and SR-X-ray absorption near edge structure (SR-XANES) spectroscopy, we successfully capture the 3D distribution of silver NPs (AgNPs) inside a single human monocyte (THP-1), associated with the chemical transformation of silver. The results reveal that the cytotoxicity of AgNPs is largely due to the chemical transformation of particulate silver from elemental silver $(Ag^0)_n$, to Ag^+ ions and Ag—O—, then Ag—S— species. These results provide direct evidence in the long-lasting debate on whether the nanoscale or the ionic form dominates the cytotoxicity of silver nanoparticles. Further, the present approach provides an integrated strategy capable of exploring the chemical origins of cytotoxicity in metallic nanoparticles.

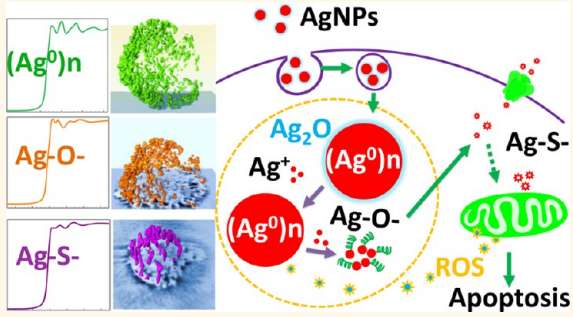

KEYWORDS: chemical origin · nanotoxicity · dynamic processes of intracellular nanoparticles · chemical transformation · AgNPs · nano-CT

Recently, critical reviews have commented on the significant weakness of the nanotoxicity studies in the past decade and suggested fields to improve in the future.[1,2] One of the most important aspects is to elucidate the underlying chemical mechanisms of nanotoxicity and clarify whether the nanoscale size of particles or their decomposition products mediate the cytotoxicity observed.[1] Silver nanoparticles (AgNPs) have been broadly used in industry, daily life, and healthcare fields.[3−5] However, reactivity of AgNPs and their potential degradation raise concerns about their biological and environmental safety.[6−9] Exposure to AgNPs *in vivo* may cause circulatory translocation and induce cytotoxic risks to monocytes, macrophages, and other blood cells,[6−8,10,11] which govern both the clearance of NPs and the immune responses to them.[13−20] AgNPs can induce oxidation stress, immune effects, genotoxicity, and apoptosis to cells,[9−12,21,22] possibly due to the changes in physicochemical properties accompanying the degradation of AgNPs.[23−25] Due to the lack of *in situ* information, how AgNPs induce these responses is still unclear. The debate is whether the AgNP toxicity mainly originates from particle-specific effects, the degraded forms of AgNPs, or the triggered oxidation stress.[17,26−28]

Nanosilver colloids in an environmental media may contain three forms of silver: Ag^0 solids ($(Ag^0)_n$), free Ag^+, and surface-adsorbed Ag^+ ions.[29−31] Both the release of Ag^+ ions[32] and the induced reactive oxygen species (ROS) in the process may increase AgNP cytotoxicity.[33,34] Therefore, controlling the Ag^+ ion release was proposed,

* Address correspondence to chenchy@nanoctr.cn.

Received for review April 25, 2015 and accepted May 20, 2015.

Published online May 20, 2015
10.1021/acsnano.5b02483

and this release was systematically slowed by thiol and citrate ligand binding, formation of sulfidic coatings, or the scavenging of peroxy-intermediates.[35,36] Nevertheless, Ag^+ ions may not be the only chemical species associated with cytotoxicity or cell death.[37] Nanoscale silver NPs may also have complicated and dynamic processes inside cells including uptake, accumulation, exclusion, and degradation into ions in the acidic endo/lysosomes, as well as chemical interactions of AgNPs or Ag^+ ions with chloride ions, thiol-containing molecules like cysteine, glutathione, proteins, and/or lipids, *etc.*[38−41] To understand whether these processes dominate AgNP cytotoxicity, we need to obtain *in situ* chemical information on silver and also correlate the physicochemical changes of intracellular NPs with the cellular responses, both in time and space.

State-of-art techniques are capable of providing chemical information including the distribution *in situ* and the chemical forms of intracellular silver. Surface-enhanced Raman scattering (SERS) imaging,[42,43] laser ablation-inductively coupled plasma-mass spectrometry (LA-ICP-MS),[44] dark field microscopic imaging,[14] focused ion beam scanning electron microscopes (FIB/SEM),[45] and so on have been employed to determine 2D distribution and accumulation of silver inside cells. With respect to microscopic images, confocal microscope has a resolution of around 200 nm to observe the spatial localization of intracellular fluorophore-labeled NPs. Transmission electron microscope (TEM) also has the advantage of ultrahigh 2D resolution (sub-nm to several nm) for detecting the local NPs in ultrathin cell slices with dozens of nanometers thickness. For nonlabeled AgNPs, chemical information-based imaging will be more powerful to visualize these NPs within cells, while single cell imaging is highly required to reveal the spatial distribution and accumulation of NPs rather than a limited 2D area. Furthermore, to characterize the chemical forms of silver, cloud point extractions assisted by ICP-MS determination,[46,47] high-resolution TEM (HRTEM),[48] X-ray photoelectron spectrum (XPS),[49,50] and fluorogenic and chromogenic probes[51] have been used to detect different species of silver like AgNPs, Ag_2S, and the soluble silver.

To better understand the cytotoxic origin, it is crucial to reveal the chemical information on silver using non-destructive chemical speciation analysis and *in situ* single cell imaging with high resolution. Recently, the synchrotron radiation (SR) transmission X-ray microscope (SR-TXM) has emerged as a novel tool especially for single cell imaging that has favorable sensitivity and high spatial resolution of tens of nanometers when equipped with phase ring and an objective zone plate.[52,53] SR-TXM is able to differentiate signals between cell background and the metallic NPs (Table S1, Supporting Information) because the low elements from cells and the heavy metallic NPs/ions absorb and refract X-rays in distinctly different ways.[54] At the beamline 4W1A of Beijing Synchrotron Radiation Facility (BSRF), TXM microscope can provide a high spatial resolution (*ca.* 60 nm) imaging with a field of view around 15 μm.[53] The monocytes have a size smaller than 10 μm, and AgNPs inside cells are suitable for high-resolution imaging under TXM. To analyze chemical information, SR-X-ray absorption near edge structure (XANES) is a sensitive fingerprint to nondestructively determine chemical species of element in complex biological samples.[55]

Herein, we studied the correlation of chemical information on AgNPs with their cytotoxic effects to human peripheral blood monocytes (THP-1). We combined SR-TXM 3D imaging and SR-XANES with measurements from conventional approaches like ICP-MS and TEM to capture key chemical information like intracellular accumulation and the changes in their chemical species. The SR-TXM imaging, together with TEM, was important to provide combined images for *in situ* 2D location and 3D accumulation of AgNPs in a cell. Then, SR-XANES, with RT-PCR and circular dichroism (CD) spectrum, was able to reveal the chemical transformation of intracellular silver. Finally, we explored the cellular and molecular responses including the changes in structure and function of organelles, apoptosis, and the signaling pathway accompanying the temporal and spatial changes of the chemical states of AgNPs.

RESULTS AND DISCUSSION

Characterization of AgNPs and Cytotoxicity. AgNPs were provided by the Institute for Health and Consumer Protection (IHCP, one Joint Research Centre of European Commission located in Italy) as a part of the European Commission's Seventh Framework Programme. Synthesized AgNPs were dispersed in Tween-20 (Figure S1A, Supporting Information). TEM images confirmed a mean size of 20 ± 3.1 nm (Figure 1A). The mean hydrodynamic size was 38.2 ± 2.7 nm as determined by dynamic light scattering in pure water (Figure S1B, Supporting Information) and the zeta potential was -4.3 ± 1.2 mV (Figure S1C, Supporting Information). Surface coating by Tween-20 maintained the AgNPs in dispersed state in pure water with close to neutral surface charge. When incubated with medium, AgNPs increased their sizes due to serum protein adsorption and partially formed small aggregates of about $d = 400$ nm (Figure 1B).

Both AgNPs and silver ions decreased the cell viability of THP-1 in a dose- and time-dependent manner as determined by CCK-8 assay, which were shown as the mitochondrial dehydrogenase activity (Figure 2A). Silver ions caused stronger toxicity than AgNPs at the same dose. The half-maximal inhibitory concentrations (IC_{50}) for AgNPs were 14.6 and 8.3 μg mL^{-1} at 24 and 48 h, respectively, while IC_{50} values for Ag^+ ions at 24 and 48 h were 5.3 and 2.9 μg mL^{-1}. Live−dead assay was also used to measure the live or dead cell ratio after

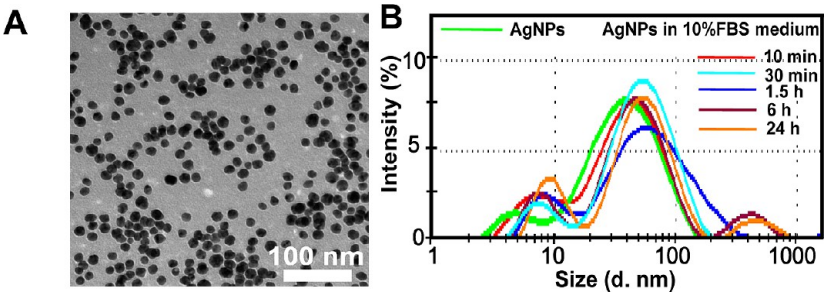

Figure 1. Characterization of AgNPs. (A) TEM image of Tween-20 dispersed AgNPs. (B) Hydrodynamic size distributions of 10 μg mL^{-1} AgNPs during 24 h in ddH_2O and 10% FBS-supplemented RPMI 1640 medium.

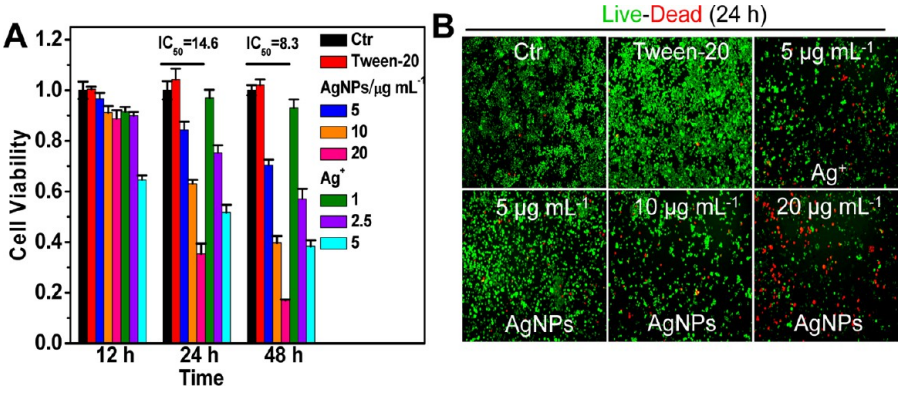

Figure 2. Cytotoxicity of AgNPs and Ag^+ ions. (A) Impacts of AgNPs, Ag^+ ions, and the dispersant (Tween-20) on the mitochondrial dehydrogenase activity shown as cell viability *vs* the dose- and time-dependence. Data are shown as mean and standard deviation (n = 4). (B) Influence of AgNPs, Ag^+ ions and Tween-20 on the percentage of live cells determined by Live−Dead assay.

the treatment (Figure 2B). The results showed that at 24 h, 10 μg mL^{-1} AgNPs and 5 μg mL^{-1} silver ions caused strong cytotoxicity and induced more cell death, which were used for the following experiments on cellular effects and the related physicochemical mechanisms.

Cellular Accumulation and Exclusion of AgNPs. THP-1 cells were exposed to 10 μg mL^{-1} AgNPs for 24 h, and the amount of silver in THP-1 cells was quantified by ICP-MS. The observed highest accumulation of silver was at 24 h (Figure 3A), which was proximate to the intracellular amount of silver at 48 h uptake (*ca.* 10.6 ± 1.3 pg/cell). Then, the cell culture medium was replaced by a NP-free medium containing 0.2% FBS to study the exocytosis process for an additional 48 h. When AgNPs in the medium was discarded, THP-1 in fresh medium (only with 0.2% FBS) could exclude silver outside cells. The direct evidence was the quantification of the secreted silver in fresh medium by ICP-MS. At such a low concentration of serum, THP-1 cells maintained a slow proliferation rate of *ca.* 5.8%. In this case, we could compare the amount of silver inside cells at 24 h uptake with that during the removal process (Figure 3A). The excluded silver was calculated by the ratio of total silver in the medium and the amount of internalized silver at 24 h. If the low proliferation rate was neglected, THP-1 cells were able to remove *ca.* 71% of the total silver 24 h later and *ca.* 82% 48 h later (Figure 3B).

3D Tomographic Imaging of AgNPs in a Single Cell by SR-TXM. At BSRF X-ray Imaging Beamline (4W1A), we employed SR-TXM to create a 3D tomographic image of AgNP locations inside a single cell. Light elements like carbon, hydrogen, oxygen, nitrogen, sulfur, chloride, sodium, *etc.* make up inorganic salts, ions, biomolecules, the components of cells, and subcellular structures. The X-ray absorption ratio and refractive index of silver are much higher than those of light elements in cells; thus, one can distinguish among silver and other elements within a cell sample (Table S1, Supporting Information). To obtain an entire data set for 3D computed tomography, 321 SR-TXM image slices were collected for the cell sample on a holder during its rotation between −80 and 80° step by step. The 2D and 3D distribution of the silver can be generated by graph segmentation, reconstruction, and cutting cell slices. To show the distribution of the silver in a single cell, the high-resolution optical information on each recorded layer of a cell was reconstructed into a 3D image by computed tomography.

Detailed three dimension reconstruction information about THP-1 cells for Control, 24 h uptake, 12 h removal, and 48 h removal should refer to the 3D animation results of Supporting Information Movies, avi files 2, 3 (Movie 12 as the phase contrast imaging result unlabeled by pseudo colors), 4, and 5, respectively.

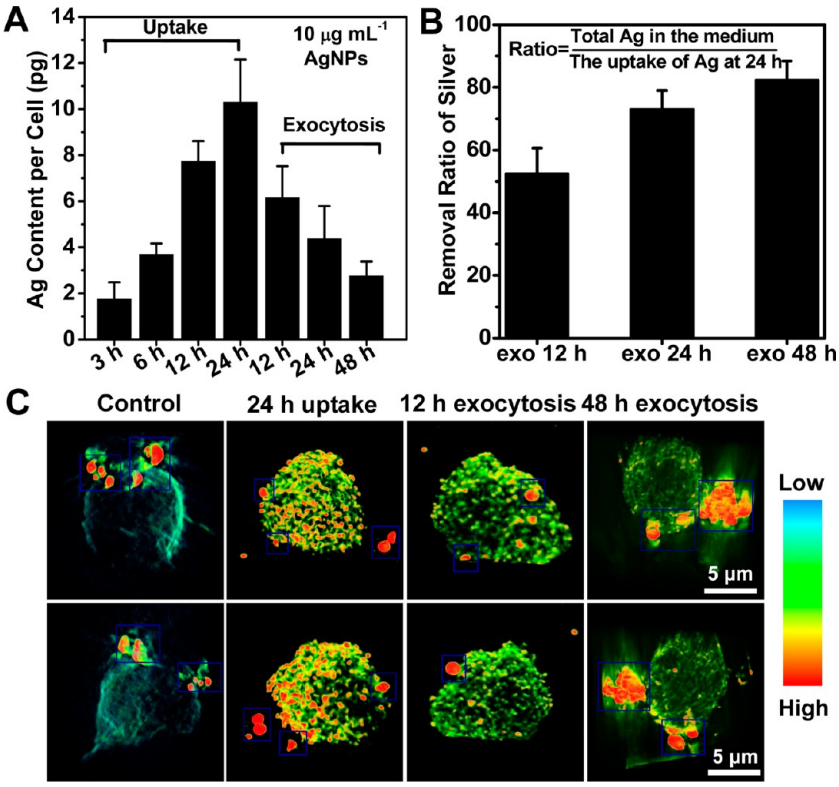

Figure 3. Cellular uptake, accumulation, and exocytosis of AgNPs. (A) Intracellular amount of silver during the AgNP uptake in a 10% FBS-supplemented medium and the exclusion of silver in a fresh 0.2% FBS medium, as determined by ICP-MS. (B) The ratio of removed silver in the free medium to the total accumulation of silver at 24 h uptake by THP-1 cells, as determined by ICP-MS. Data are shown as mean and standard deviation (n = 4). (C) The spatial distribution of AgNPs in a single cell captured by SR-TXM. Smaller colored spots indicate particles or vesicles on the surface or inside the cells. Green, yellow, and red colors indicate increasing gradients of X-ray absorption intensity by vesicles or aggregated particles. The larger red particles in the square blue frames are gold particles used as a reference for data reconstruction-processing. The color bar indicates the related contrast signals from X-ray absorption of silver inside cells. The detailed information extracted from the 3D tomography of AgNPs in a single cell is also shown for 24 h uptake (Supporting Information Movie, avi files 6,7,8, and 12) and for 48 h exocytosis (Supporting Information Movies, avi files 9,10,11).

After image segmentation, the results can be shown as rotation, 2D slice, and 2D projection modes. The 24 h uptake results were shown as Supporting Information Movies, avi files 6, 7, and 8, respectively, whereas the 48 h exocytosis results were shown as Supporting Information Movies, avi files 9, 10, and 11, respectively. To show the locations of AgNPs on the cell membrane or in the cytoplasm, we showed several random series of slices in a single cell at 24 h uptake from the raw data of SR-TXM phase contrast images (Figure S4, Supporting Information). As shown in Figures 3C and 4, SR-TXM images clearly indicate the accumulation of silver followed by exocytosis, which is consistent with the ICP-MS results (Figure 3A,B). According to random slices of TXM phase contrast images (Figure S4, Supporting Information), we observed that at 24 h uptake most of AgNPs were located in the cytoplasm, in accordance with other reports (based on TEM) that AgNPs are mainly located in the endosomes and the lysosomes.[13,19,22]

A comparison of this spatial distribution of silver is shown in Figure 3C, where the blue pseudo color represents the cell background and the yellow, red, and green colors represent silver-containing vesicles sized in a 200−600 nm range. The highest accumulation was observed at 24 h, as illustrated by the number of colored vesicles or spots (Figure 4A1−7 and B1−7; Supporting Information Movie, avi file 2 as control, and avi file 3 at 24 h uptake). During exocytosis, the intracellular concentration of silver decreased with time (Figure 4C1−7 and D1−7, Supporting Information Movie, avi file 4 at 12 h removal, avi file 5 at 48 h removal), as shown by the decreasing number of bright vesicles or spots. The AgNPs accumulated at a 24 h uptake (Figure 4A1−7) was shown as purple spots. Random internal slices may be observed from three directions: the *xy*, *xz*, and *yz* planes. From the representative cell cross sections, we observed that the purple spots indicating AgNPs were encircled by the gray vesicles (Figure 4B1−7). The actual contact area of silver on the slices can be seen as purple spots on the random white 2D plane. AgNPs was preferentially located in the cytoplasm close to the cell membrane and around the center (nucleus) (Figure 4A3, B3; A5, B5; Figure S4 and Movie avi file 12 in Supporting Information).

During uptake and exocytosis, the accumulation and localization of AgNPs could also be observed by

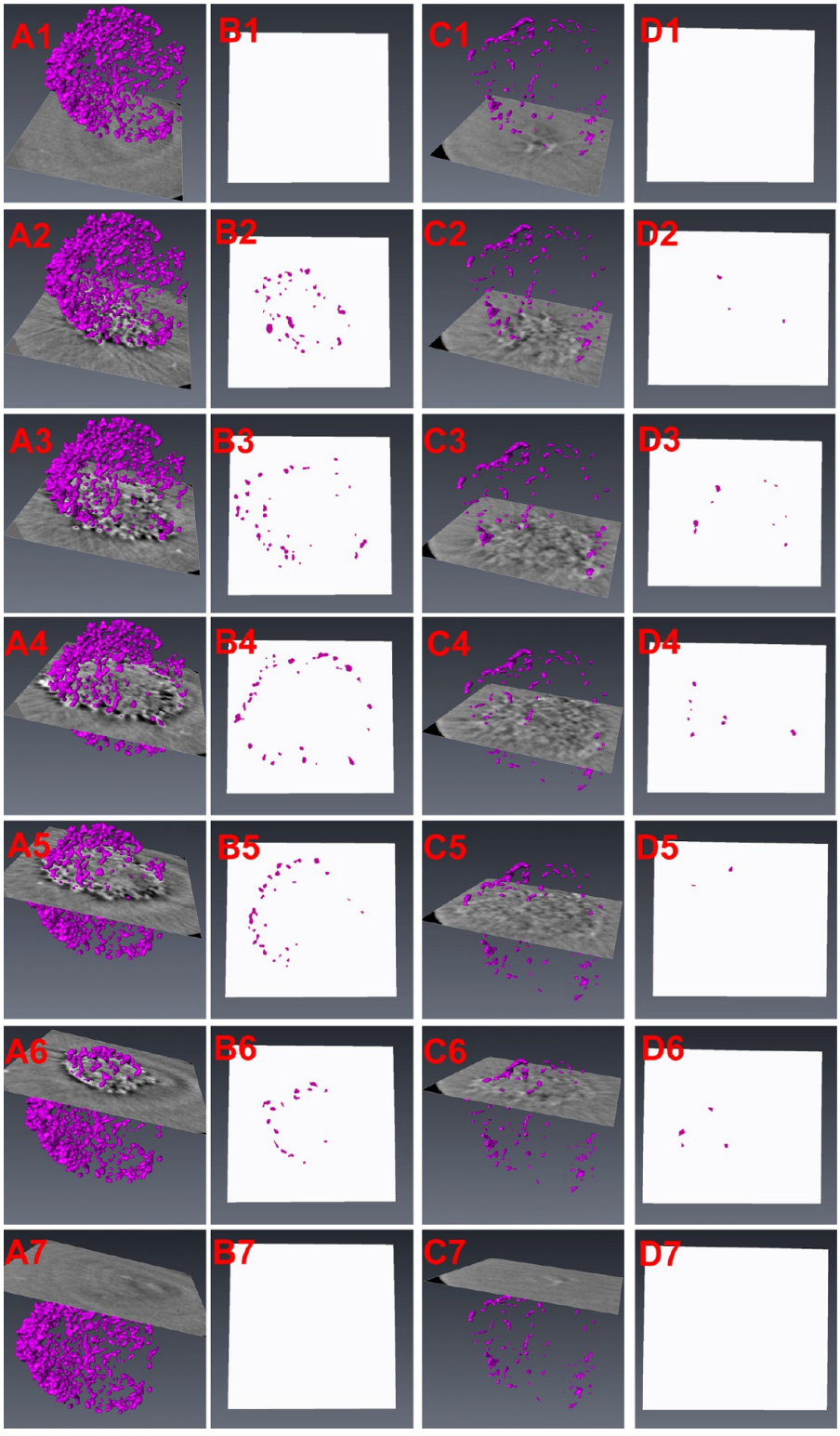

Figure 4. 3D tomographic images of AgNPs within a single THP-1 cell. Two representative series of cross sections from the bottom up of single cells that have internalized AgNPs for 24 h (A1−7) and undergone exocytosis for 48 h (C1−7), respectively. The projected spots on the gray sections indicate the contact area of silver-containing vesicles. 2D distribution information on AgNPs corresponding to the 3D tomography is indicated by the purple spots on each white cross section for uptake process (B1−7) and exocytosis (D1−7).

TEM. After a 24 h uptake, TEM images showed that AgNPs were mainly localized at vesicles such as the endosomes or the lysosomes with differing sizes of AgNPs (Figure 5A). AgNPs were not observed to locate at the mitochondria and the nuclei; however, the mitochondrial structure changed and became swollen

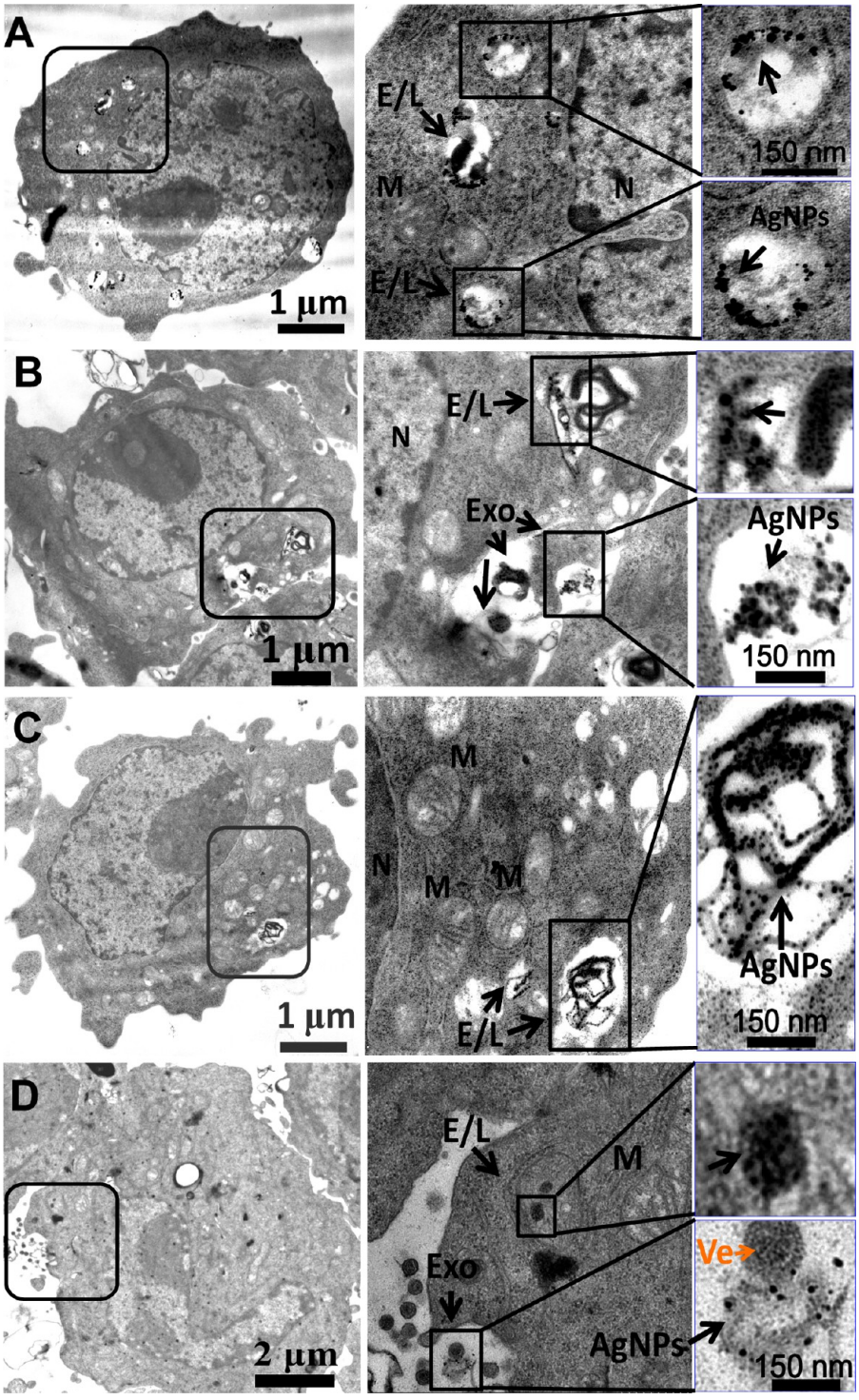

Figure 5. TEM images of AgNPs within and around THP-1 cells. (A–D) TEM images of cells and AgNPs after a 24 h uptake of AgNPs (A), followed by 12 h (B), 24 h (C), or 48 h (D) of exocytosis. For each figure on the left, representative images are shown in zoomed insets. The capital letters N, M, E/L, Exo, and Ve are short for the nuclei, the mitochondria, the endosomes/lysosomes, the structures for exocytosis, and the vesicles to remove silver, respectively. In panel D, the orange arrowhead points to the vesicle that removes AgNPs and the black arrowhead shows AgNPs.

and round (Figure 5A, Figure S2 in Supporting Information). During exocytosis, AgNP-containing vesicles were also secreted by THP-1 cells (Figure 5B–D), while a part of expelled AgNPs seemed to be included in vesicles or close to them (Figure 5B,D). The removal of AgNPs restored the subcellular structures. At 48 h of exocytosis, fewer vesicles could be observed in the cells than at 24 h, and the number of mitochondria with normal shape and morphology also increased (Figure 5C,D). The use of uranyl acetate in solution (pH 4.0) to stain cells may lead to the dissolution of AgNPs; therefore, it is difficult to confirm the dissolution

of AgNPs inside cells directly from a TEM image. However, TEM combined with other sensitively analytical techniques, such as XANES, makes it possible to characterize the degradation of AgNPs.

To view the accumulation and the removal of silver for a whole cell, SR-TXM 3D imaging is more informative than TEM images with 2D cell sections. 2D (a variety of cell slices) and 3D (in a whole cell) views of AgNPs in a single cell provide *in situ*, sensitive, nondestructive, and high-resolution images of intracellular NPs. On the basis of 2D localization and 3D distribution of AgNPs, AgNP toxicity is possibly due to the accumulation of silver, in accordance with other reports.[28]

Chemical Transformation of Silver in the Cells. In the acidic endosome and lysosome system, AgNPs may be degraded into ions[25,31] and may generate ROS.[56] However, the ionic silver is not a stable form in a biological system and it may react with ligands like Cl^-, Br^-, thiols, peptides, or proteins.[41,57,58] To detect these chemical forms, we employed SR-XANES, a powerful technique to characterize elemental speciation in complicated biological samples.[59,60]

On the basis of silver K-edge XANES, five reference samples for silver such as Ag foil (elemental Ag), Ag_2O, Ag_2S, AgCl, and $AgNO_3$ (for Ag^+ form) were used to fit XANES results of test samples. The shapes of XANES spectra are quite different for different silver reference samples, *e.g.*, the peak shapes for Ag−S− (a flat peak) and $(Ag^0)_n$ (a sharp peak) are quite distinct. The shape of the XANES peak for AgNPs was similar to that of Ag foil, but changed to that of Ag−S− during internalization and exocytosis, which was consistent with the fitted data for Ag species (Table 1). The least-squares fitting results showed that the original AgNPs contained 93.1% elemental Ag and 6.9% Ag−O− (Figure 6A), providing that surface of the silver NPs had been oxidized before uptake. During the uptake and exocytosis, XANES results and the data fitting clearly showed changes in silver chemical forms (Figure 6B, Table 1), indicating that AgNPs were gradually transformed into Ag−O− and then Ag−S− forms. For the accumulated AgNPs, the fluctuation of the Ag−O− ratio suggests that Ag−O− is a midproduct between $(Ag^0)_n$ and Ag−S−. Inside the cells, the exposure to cysteine, cystine, and methionine moieties of the abundant peptides, proteins and other antioxidant molecules such as metallothioneins (MTs) may provide abundant sulfur sources to coordinate with silver.[61,62]

The transformation of silver inside cells is a complicated process. In the presence of organic acids, silver atoms on the surface of AgNPs can degrade into ions and Ag−O− species that subsequently bind to thiols derived from sulfur-containing molecules. The stability of Ag−S− is stronger than Ag−O− due to the dissociation constant of Ag_2S which is about $K = 10^{-50}$; the characteristics in dissociation constant drive more silver ions to thiols.[57] The degradation of AgNPs can also induce ROS.[56] Both ROS and dissolved oxygen oxidize the surface silver into Ag_2O (Ag−O− speciation).[48] Then, the dissolution of Ag_2O into ions, possibly binding to organic acid molecules (Ag−OOC−R), and then generation of Ag−S− by

TABLE 1. Time-Dependent Changes in Sliver Species inside THP-1 Cells Based on Silver K-Edge XANES

	chemical forms and the ratio (%)				
	$(Ag^0)_n$	Ag−O−	Ag−S−	Ag^+	AgCl
AgNPs	91.9 ± 2.3	9.1 ± 2.5	0	0	0
12 h uptake	60.8 ± 3.8	32.8 ± 2.1	0	6.4 ± 1.3	0
24 h uptake	43.4 ± 3.1	26.3 ± 1.5	33.1 ± 2.7	0	0
12 h exocytosis	40.5 ± 2.5	15.8 ± 1.7	44.7 ± 3.3	0	0
24 h exocytosis	35.4 ± 2.2	0	64.6 ± 4.2	0	0
48 h exocytosis	21.4 ± 3.3	0	78.6 ± 5.1	0	0

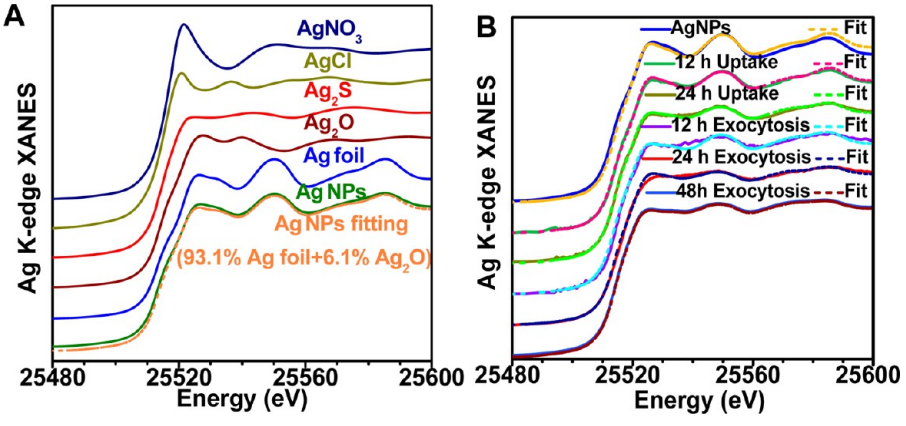

Figure 6. Chemical transformation in silver species inside THP-1 cells. (A) Chemical species of silver in reference samples and AgNPs as determined by silver K-edge XANES. (B) Changes in silver chemical species of the cell samples during the cellular uptake of AgNPs and the removal of silver according to silver K-edge XANES. The uptake process indicates a continuous exposure to 10 μg mL^{-1} AgNPs for 12 or 24 h, while the exocytosis process shows an additional 12, 24, and 48 h after a 24 h uptake.

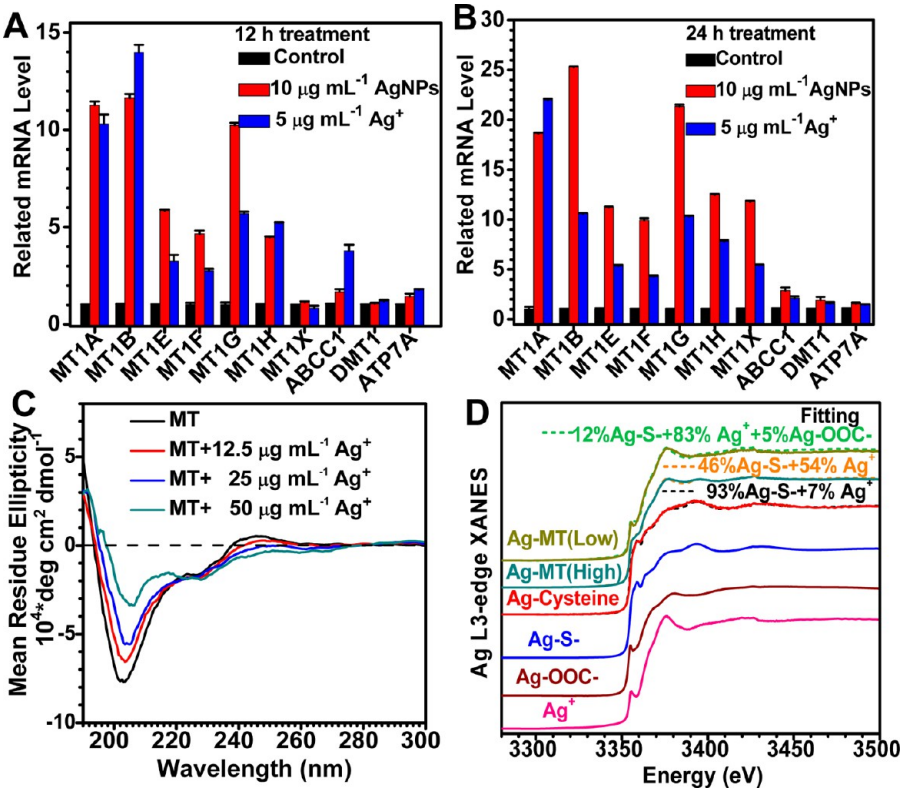

Figure 7. Gene modulation of THP-1 cells by AgNPs and the change in secondary structures of MT protein exposed to Ag^+ ions. (A and B) Changes in mRNA level of the metal chelation and exporting-related genes after the exposure to AgNPs or Ag^+ ions for 12 h (A) and 24 h (B). MT families are responsible for chelating metal ions, while ABCC1, DMT1, and ATP7A play roles in exporting metal ions or compounds. Data are presented as mean value and standard deviation (n = 3). (C) Changes in secondary structures of MT during its interaction with Ag^+ ions as measured by CD spectra. (D) Characterization of silver speciation according to Ag L_3-edge XANES when Ag^+ ions bind MT-1 protein. XANES data are normalized and described as the ratio of different species.

interacting with thiol-containing proteins or polymers (such as polyethylene glycol thiol) probably drive the degradation of AgNPs by forming more stable species.[41,57,63−65] At 12 h uptake, almost 40% of AgNPs were oxidized to Ag−O− species (32.8%) or degraded into silver ions (6.4%) with an elevated ROS level (discussed later). At 24 h uptake, even more AgNPs turned out to be Ag−O− (26.3%) or Ag−S− species (33.1%). During exocytosis for 48 h, the percentage of elemental Ag (21.4%) decreased, while most of the silver existed as Ag−S− (78.6%) (Table 1). One possible mechanism is that cysteine or cysteine-containing peptides may be bound to the AgNP surface to induce its further oxidation and binding to carboxy groups to form Ag−O−, subsequent dissolution, and exocytosis.[24,41,64]

Furthermore, the molecular biological results provide evidence to correlate chemical transformation of NPs to the exclusion of silver and cytotoxicity. Previous proteomic or global gene expression profiling studies showed that the exposure to AgNPs or Ag^+ ions may activate pathways that are associated with oxidation stress,[19,66,67] metal transport systems and detoxification.[34,61] In general, metal transport proteins or genes including ATP-binding cassette transporter subfamily C member C1 (ABCC1), divalent metal transporter 1(DMT1) and copper-transporting ATPase 1 (ATP7A) are responsible for transporting or excluding metal ions and metal-bound molecules.[34,38,68,69] We found that THP-1 cells significantly increased mRNA expression of these genes during the uptake and the removal of silver (Figure 7A,B, Figure S3A,B in Supporting Information). DMT1 is responsible for both the cellular intake of metals and the release of metals into cytoplasm from the lysosomes.[68] During the uptake and exclusion processes, the higher levels of DMT1 mediated the release of degraded forms of silver from the lysosomes to the cytoplasm. Cysteine-containing biomolecules such as MTs may directly bind Ag−O− in the cytoplasm to form Ag−S− bond. Proteins of MT family are mainly located in the cytoplasm and contain 20 cysteine residues to bind metal ions in order to reduce toxicity.[70] In this case, exposure to AgNPs induced 5-fold increase of mRNA level of MTs at 12 h and 10-fold at 24 h, in accordance with other reports.[61,62,71,72] Binding of silver to MTs was indirectly supported by changes in the secondary structures of MT by circular dichroism (CD) spectra (Figure 7C and Table 2). Cysteine residues in MTs were bound to

dissolved silver to form Ag—S— bonds as indicated by Ag L_3-edge XANES spectra (Figure 7D).

ABCC1 and ATP7A metal transporters may also play a role in exporting intracellular silver (Figure S3A,B, Supporting Information). THP-1 cells responded to silver ion exposure by elevating expression of ABCC1 and ATP7A-related proteins (Figure S3A, Supporting Information). However, expression of other exporter genes such as ATP7B and vesicle secretion-related TRAPP3 did not change after treatment with AgNPs and/or silver ions. Therefore, the soluble Ag—S— form might be a form of silver for monocytes to remove. We speculate that binding of soluble silver to the cell membrane/organelle structure proteins and enzymes in mitochondrial respiratory chains triggers toxicity.

TABLE 2. Changes in Secondary Structures of MT Protein That Interacts with Silver Ions[a]

	secondary structures of MTs			
concentration of Ag^+ mixed with MTs	α-helix	β-sheet	β-turn	random
0	2.5%	49.9%	0	47.6%
12.5 μg mL^{-1}	4.8%	47.8%	0	47.4%
25 μg mL^{-1}	8.2%	48%	0	43.8%
50 μg mL^{-1}	23.1%	18%	8.7%	50.2%

[a] In PBS (pH 7.2, chloride ion-free) and at room temperature, 0.2 mg mL^{-1} MT is incubated with silver ions at different concentrations for 30 min. To measure the CD signals of MT in the mixture, the secondary structure information shows the binding of MT with silver ions.

Cellular Responses to AgNP Exposure. With the dissolution of AgNPs, both ROS and the interaction between soluble silver (Ag^+ and Ag—O—) and thiol-containing molecules may induce structural and functional changes in THP-1 cells. Live—Dead assay showed that AgNPs above 10 μg mL^{-1} directly caused cell death as compared with 5 μg mL^{-1} of silver ions, suggesting that the cytotoxicity of AgNPs was partially caused by the ionic form of silver (Figure 8A). Once located at the lysosomes, the degradation of AgNPs caused leakage of the lysosomal membrane as determined by an AO assay (Figure 8B), although AgNPs and Ag ions induced less lysosomal membrane permeation (LMP) than a positive control drug polyethylenimine (PEI).[73] But both could induce impairment in lysosomal membranes in a dose-dependent fashion. Moreover, silver ions decreased the integrity of the lysosomal membranes more than AgNPs did, partly because the

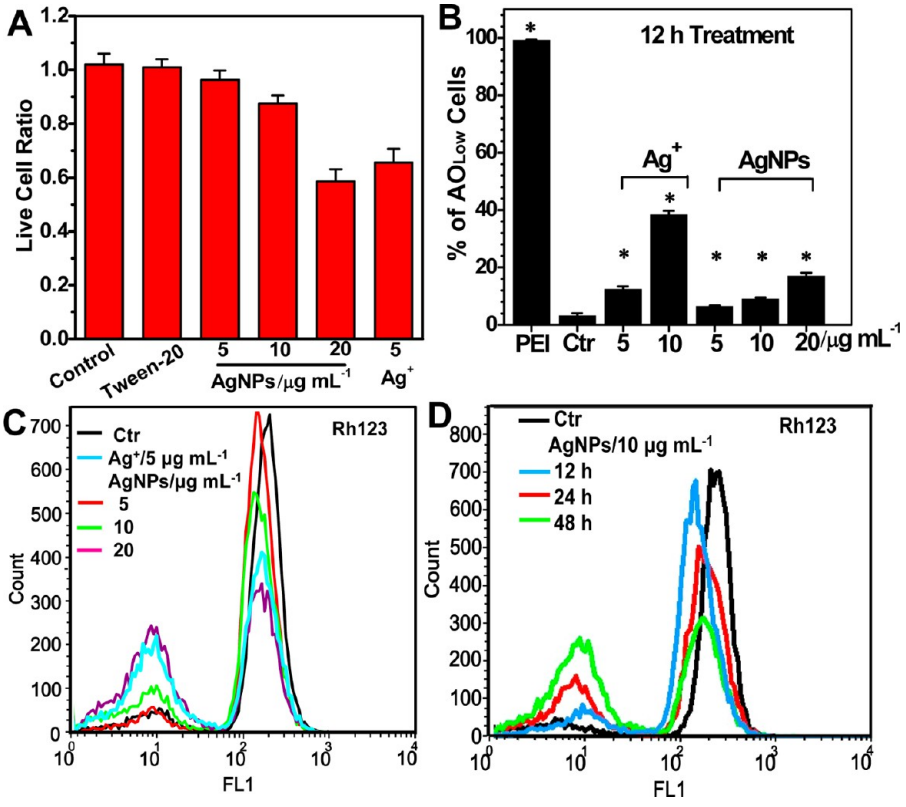

Figure 8. Influences of AgNPs and Ag^+ ions on cell death, lysosomal membrane permeation (LMP), and mitochondrial membrane potential (MMP). (A) Impacts of AgNPs, Ag ions, and Tween-20 on cell survival and death using Live—Dead assay. Data are shown as mean value and standard deviation (n = 4). (B) Dose-dependent change in the lysosomal membrane integrity when cells are expose to AgNPs or Ag^+ ions for 12 h, as determined by AO assay. Treated with 2 μg mL^{-1} polyethylenimine (PEI), THP-1 cells are used as a positive control. Data are shown as mean value and standard deviation (n = 3). The asterisks represent significant differences between the control and test samples (p < 0.05). (C) Changes in the MMPs after a 24 h exposure to AgNPs or Ag^+ ions, as determined by Rhodamine 123 fluorescence intensity. (D) Time-dependent change in the MMPs when cells are exposed to 10 μg mL^{-1} AgNPs.

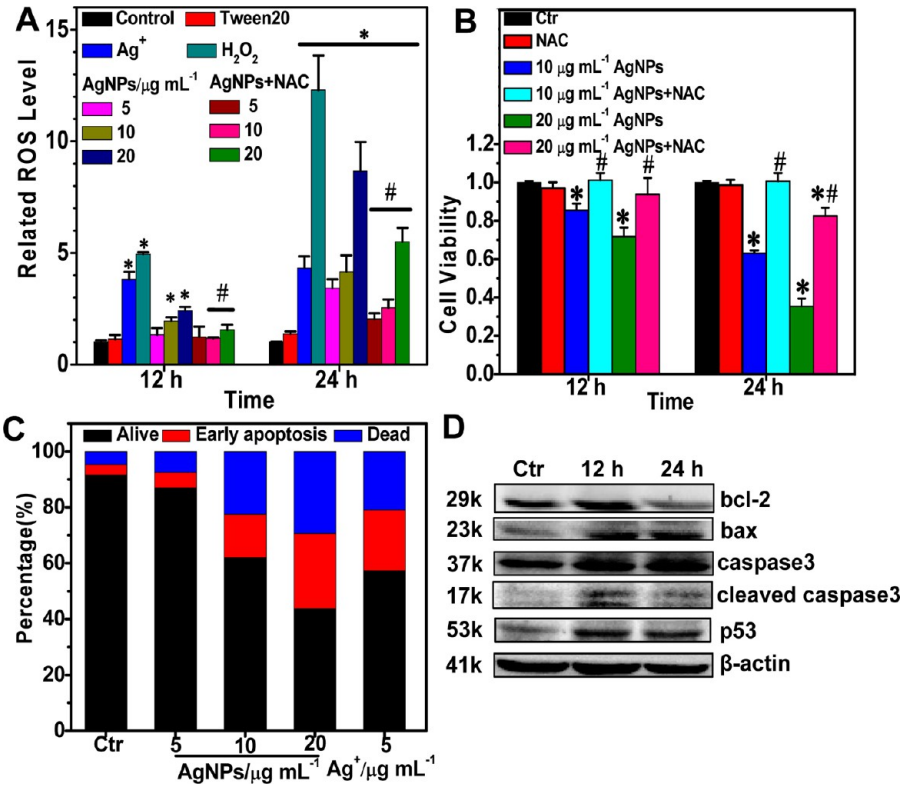

Figure 9. Influence of AgNPs on the oxidative stress level, cell viability, and apoptosis. (A) Intracellular ROS level determined by DCFHDA with flow cytometry. (B) Influence on the mitochondrial dehydrogenase activity when cells are exposed to AgNPs with or without NAC for 12 and 24 h. (C) Proportion of the early apoptosis and death induced by AgNPs and Ag^+ ions after 24 h exposure, which is based on flow cytometry. (D) Change in the apoptosis-correlated proteins after 12 or 24 h exposure to 10 μg mL^{-1} AgNPs. Data are shown as mean and standard deviation ($n = 3$). The asterisks (*) represent significant differences between the control and test samples ($p < 0.05$), while the pound signs (#) indicate significant differences between AgNP-treated THP-1 cells supplemented with NAC or not ($p < 0.05$).

exposure to silver ions is an immediate effect, while the release of ions from AgNPs is a time-dependent process.

Not only is the lysosome a digestive organelle, but it is also involved in the lysosome-mediated apoptosis *via* a ruptured lysosomal membrane, which releases hydrolytic enzymes to trigger mitochondrion-mediated apoptosis.[73,74] We measured the changes in the mitochondrial membrane potentials (MMPs) with a flow cytometry using the Rhodamine 123 (Rh123) assay, where cells with lower MMPs accumulate less fluorescent Rh123. We found that AgNPs reduced MMPs in a dose- and time-dependent manner (Figure 8C,D). Ag ions at 5 μg mL^{-1} concentration resulted in effects comparable to those of 10 μg mL^{-1}AgNPs, suggesting that the degradation of AgNPs into ions partially contribute to reduced MMP levels (Figure 8C). At 24 h, both silver ions and AgNPs decreased MMPs, which constitutes an early event to trigger apoptosis.

Usually, decreased MMP generates a substantial amount of ROS.[75,76] Both Ag^+ ions and AgNPs elevated intracellular ROS levels at 12 and 24 h (Figure 9A). AgNPs produce both time- and dose-dependent ROS. The level of ROS induced by AgNPs was lower than Ag^+ ions after 12 h exposure, while both of them were approximate after 24 h exposure. Mitochondrial dehydrogenase activity is also influenced by MMPs and is positively correlated with cell viability. When THP-1 cells were exposed to AgNPs, cell viability decreased with time (Figure 9B), and the inhibition effects of 5 μg mL^{-1} Ag^+ ions on cell viability are comparable to 10 μg mL^{-1} AgNPs. After exposure to AgNPs, a ROS inhibitor, *N*-acetyl-cysteine (NAC), lowered the cellular ROS levels inside THP-1 cells and restored their viability, indicating that the induced ROS contributed to cytotoxicity of AgNPs. Therefore, both AgNPs (10 μg mL^{-1}) and Ag^+ ions (5 μg mL^{-1}) induced approximate cytotoxic effects probably due to the degradation of AgNPs and the release of soluble silver companying with ROS generation.

Next, we evaluated the apoptosis ratio after treatment either with AgNPs or Ag^+ ions. Flow cytometry results showed that both induced early apoptosis of THP-1 cells, and Ag^+ ions at 5 μg mL^{-1} cause an effect intermediate between those of AgNPs at 10 and 20 μg mL^{-1} (Figure 9C). In accordance with the above results regarding LMP, MMPs, ROS, and cell viability, the apoptosis result showed that AgNPs are less toxic than silver ions.

Detailed molecular events including the regulation of bax, caspase 3, bcl-2, and p53 expression are involved

in the activated apoptosis process (Figure 9D). At 12 h, AgNPs elevated ROS levels and promoted the expression of bcl-2 for survivor. At 24 h, cells failed to protect themselves from the degraded silver, and thus, the strong oxidative stress caused a decline in the expression of bcl-2, along with elevated p53 expression. Moreover, both the degraded silver and ROS can induce cell damage, which increased the expression of bax and provoked bax-mediated apoptosis. Then, bax activated caspase 3 by increasing the cleavage of caspase 3, which then executed the apoptosis program. Therefore, both the cellular and molecular events indicate that AgNPs can induce apoptosis as a result of their degradation and an elevated level of ROS.

Due to the complexity of a cell sample, it is a grand challenge to capture *in situ* chemical information on NPs inside a nondestructive cell. To this end, some pioneering efforts have been made, for example, FIB/SEM complemented with energy-dispersive X-ray spectroscopy was employed to observe the cellular uptake and the intracellular distribution of agglomerated AgNPs.[45] This method requires cutting a cell using ion milling in order to visualize the intracellular particles. LA-ICP-MS microbeam mapping was used as an *in situ* but destructive technique to detect silver in a single cell with a beam size area of several micrometers squared (μm^2).[44] Meanwhile, SERS imaging technique was also used obtain *in situ* and nondestructive information for protein or cysteine-bound AgNPs, which could map intracellular AgNPs in 2 μm steps.[43]

The use of SR coherence monochromatic X-rays and energies tunable from soft to hard X-rays is beneficial for studying a cell−NP interaction system. The recent development of zone plates also allows a much smaller beam focus and improves the spatial resolution up to tens of nanometers,[77,78] a suborganelle level. SR-TXM is capable of nondestructive and single cell imaging; however, the planar resolution of SR-TXM images is lower than that of TEM, and SR-TXM can hardly distinguish single nanoparticle in sizes of several tens of nanometers. To overcome this disadvantage, we here integrated SR-TXM with TEM to reveal both the overall and the local accumulation and dynamic translocation of silver inside a cell. In some previous studies, AgNP aggregates within vesicle structures of cells were determined by combining 3D cryo-soft X-ray tomography (cryo-SXT) and TEM techniques.[42,43] The cryo-SXT imaging was performed under a water window with K-edge binding energies for carbon (284 eV) and oxygen (543 eV), where water is relatively transparent, so the organelle or membrane structures and metallic NPs were visualized.[54,79,80] The soft X-ray has a penetration depth less than 10 μm, and provides only partial imaging of a cell sample with a less contrast to metallic NPs.[42,43] The use of hard X-ray (at 8000 eV) in TXM imaging has a capacity to penetrate a thicker sample for visualizing NPs in three dimension of a whole cell. The limitation of hard X-ray is its transparency to subcellular vesicle due to its less contrast for carbon and oxygen elements. So, a perfect approach is to integrate the cryo-SXT 3D imaging (preferred for cellular components) and SR-TXM 3D imaging (preferred for metallic NPs) for cell−NPs samples. This integration needs the development of an interface system to correlate the information obtained from these two imaging approaches.

With SR-XANES, we are able to reveal chemical information about silver speciation accompanying intracellular dynamic processes. When equipped with multiple element solid detectors, SR-XANES has a detection limit of several parts per million (ppm) and is capable of determining chemical speciation composition of silver element inside cell samples with high sensitivity. SR-XANES can provide chemical forms of intracellular silver to understand the degradation and transformation of AgNPs. On the basis of SR-XANES, a previous work demonstrated that silver within AgNP and Ag^+ ion-exposed *Caenorhabditis elegans* worms was complexed with sulfur atoms,[81] in accordance with our result.[25] Importantly, SR-XANES also renders the study about interaction of Ag^+ ions with sulfur-containing molecules in a solution possible. We further capture the possible target of dissolved Ag^+ ions by combining SR-XANES to characterize the interaction between protein molecule and Ag^+ ions with molecular approaches.

It is crucial to correlate the chemical information with key cellular events like LMP, MMPs, ROS generation, and the activated apoptosis pathway, *etc.*, which is helpful to understand mechanism of nanoparticle cytotoxicity. The present data from advanced synchrotron technology and toxicological approaches suggest that the temporal transformation of intracellular AgNPs from their particulate form of $(Ag^0)_n$, to Ag^+, Ag−O−, and Ag−S− species plays key roles in producing their cytotoxicity. Soluble silver inside cells can cause the impairment in structures of lysosomes and induce dysfunction of mitochondrion to trigger apoptosis. The change in the expression of apoptosis proteins like bcl-2, bax, and p53 revealed this dynamic process. Bcl-2 is a survival protein that partly resides on the mitochondrial outer membrane and prevents the mitochondrial release of cytochrome c (Cyt c) to trigger apoptosis. Bcl-2 protects the cell against toxic stimuli, but a strong stimulus to activate apoptosis can downregulate its expression.[82] When bcl-2 proteins sense cell damage stimulus, bax and bax-like proteins are critical downstream mediators of apoptosis that promote the mitochondrial permeability transition and permeabilize the mitochondrial outer membrane to release Cyt c. The Cyt c then induces activation of proteases such as caspases to demolish the cell.[83] In addition, p53 is a tumor repressor that mediates apoptosis after DNA damage induced by genotoxic

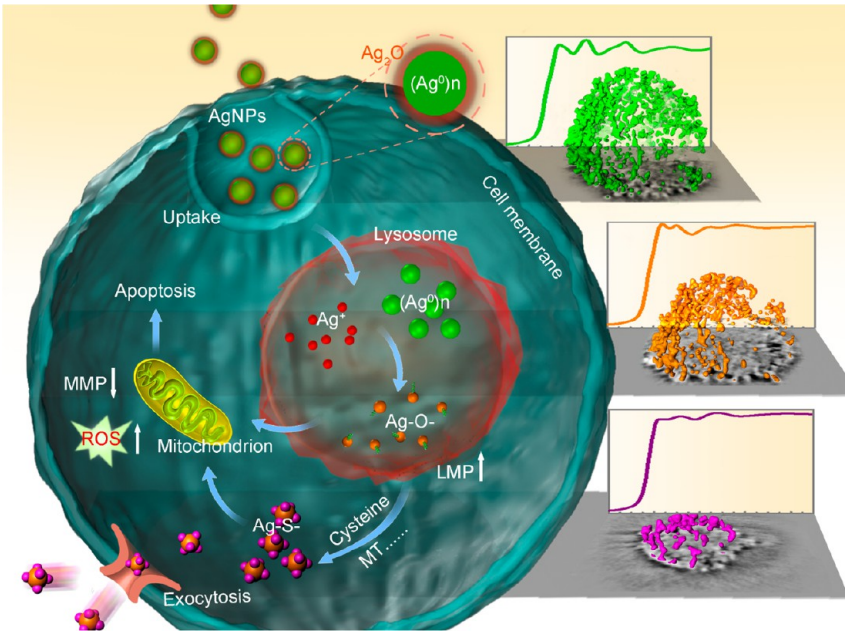

Figure 10. A schematic diagram of chemical mechanism of AgNP toxicity to human monocytes (THP-1). AgNPs are internalized by cells and trafficked from engulfed vesicles to the lysosomes. Due to the acidic environment in the lysosome, AgNPs in the form of $(Ag^0)_n$ are dissolved into Ag^+ ions and then changed into Ag−O− form possibly due to the binding of organic acid molecules. Dissolved silver increases LMPs that leads to the release of both dissolved silver and lysosomal contents to the cytoplasm. Then, both the increased LMPs and the released silver decrease the mitochondrial membrane potentials, which results in ROS generation and cell apoptosis. Meanwhile, the dissolved silver (Ag−O−) will interact with cysteine-contained proteins like metallothioneins, enzymes, *etc.* to become Ag−S− speciation, which may trigger mitochondrion-involved apoptosis. However, a part of Ag−S− form may be exported by the membrane transporters to reduce cytotoxicity. To understand the chemical origin of AgNP cytotoxicity, two advanced techniques are powerful to illustrate the dynamic processes of intracellular AgNPs in time and space. SR-TXM can *in situ* study the intracellular accumulation and exocytosis of AgNPs, while SR-XANES is capable of revealing the chemical transformation of silver from the oxidation and degradation to the Ag−S− form.

drugs and radiation.[84] p53 regulates the intracellular redox state and induces ROS-dependent pathways to apoptosis,[84] and the translocation of p53 into the nuclei can be interfered with by bcl-2.[85]

CONCLUSIONS

In summary, we demonstrated that the chemical origin of AgNP cytotoxicity is largely due to their chemical transformation resulting in dynamically chemical and biological changes inside a cell (Figure 10). We applied SR light source-based TXM with 3D tomographic imaging and XANES to clarify whether AgNPs or the degraded silver play major roles in determining the cytotoxicity of AgNPs. The integrated techniques successfully captured key chemical and biological information on AgNPs during cellular uptake, accumulation, degradation, chemical transformation, and removal. The spatial distribution and intracellular translocation of silver in a single cell has been captured by TEM and SR-TXM with 3D tomographic imaging; meanwhile, the SR-XANES revealed the temporal transformation of AgNPs from $(Ag^0)_n$ to Ag^+, Ag−O−, and Ag−S− species. This new evidence well correlates with key events of cytotoxicity including upsetting integrity of the lysosomal membranes, decreased MMPs, induced ROS-generation, and finally apoptosis. Our study indicates that particulate form of AgNPs, their degraded forms, and the induced ROS play synergetic roles in mediating AgNP cytotoxicity to human monocytes. In addition, the present study provides us with an advanced approach for nondestructive detection of intracellular NPs. It provides direct information to reveal the origin of nanotoxicity and also helps us understand biomedical interactions of nanomaterials and their possible mechanisms in nanosafety assessments and application fields.

MATERIALS AND METHODS

Cell Culture. Human acute monocytic leukemia cell lines (THP-1) were obtained from ATCC and cultured in a complete medium (RPMI 1640 medium containing 10% fetal bovine serum (FBS, GIBCO) and streptomycin/penicillin (100 μg mL^{-1} or 100 U mL^{-1}, Hyclone) at 37 °C in a moisturized 5% CO_2 incubator.

Characterization of AgNPs. AgNPs were provided by the European Commission Joint Research Center (Ispra, Italy). AgNPs (10% silver, w/w) were dispersed by 4% (w/w) Tween-20 in water. For long-term storage, AgNPs were placed in a brown reagent bottle filled with nitrogen, protected from light, and stored at 4 °C in a refrigerator. AgNPs were observed under a transmission electron microscope (TEM, FEI Tecnai G-2).

The mean hydrodynamic sizes and the surface charges of AgNPs were measured by zeta potential and dynamic size analyzer (Malvern Zeta Sizer Nano ZS), as was shown by zeta potential and a mean size distribution, respectively. To study the states of AgNPs during exposure, we incubated 10 μg mL^{-1} AgNPs in a complete medium at 37 °C for different time spans and measured the hydrodynamic sizes. In Tween-20, most AgNPs keep stable and undissolved states for at least two years based on XANES and ICP-MS. The fitting results of silver K-edge XANES show 93.1% and 91.6% element silver in colloidal dispersion for as prepared AgNPs and those after two year storage.

Cytotoxicity Assay. A mitochondrial-based cell viability assay, MTT, was used to measure cytotoxicity. Cells (5×10^4 cells/well) were seeded in 96-well microplates (Corning, Costar, NY) containing 200 μL of cell culture medium and were exposed to AgNPs (0, 5, 10, and 20 μg mL^{-1}) and Ag^+ ions (1, 2.5, and 5 μg mL^{-1}) for 12, 24, and 48 h, respectively. After treatment, the mixture of 10 μL of 5 mg mL^{-1} MTT in PBS and 100 μL serum-free DMEM was added to each well for 3 h. The 96-well microplate was centrifuged 5 min at 5000 rpm to precipitate cells. The supernatant was discarded and 100 μL of DMSO was added to each well. The absorbance was measured at 570 nm using Infinite M200 microplate reader (Tecan, Durham, NC). Viability/Cytotoxicity Kit (Molecular Probes) was also used to study the cytotoxicity. Cells were seeded in 96-well microplates and exposed to AgNPs and Ag^+ ions. These cells were stained with calcein/AM and thidium homodimer for 30 min. The live cells were stained green by calcein, while the dead ones were stained red by PI. The stained cells were observed under an inverted fluorescence microscope (Olympus, Japan), which were excited at 488 nm with emission at 537 nm for calcein (green), and excitation at 561 nm with emission at 615 nm for PI (red). The ratio of dead cells to total ones was evaluated by the value of Count red/Count$_{\text{green + red}}$.

Determination of AgNP Uptake and Exocytosis. To study cell uptake, cells (2×10^5 cells/well) in 6-well plates were exposed to 10 μg mL^{-1} AgNPs for 3, 6, 12, and 24 h in a complete medium. To study exocytosis, after 24 h exposure to 10 μg mL^{-1} AgNPs, cells were rinsed with PBS and further cultured 24 and 48 h in a 0.2% FBS medium. Each sample had four replicate wells. After a rinse step with PBS three times, cells were collected, counted, and centrifuged. A 5 mL volume of HNO_3 was added to sample overnight as was transferred to a conical flask with 2 mL 30% H_2O_2. Placed onto a hot plate, flasks were maintained 3 h at 150 °C to digest silver to be ions. The products were cooled to room temperature and diluted to 3 mL 2% HNO_3 solution. A 10 ng mL^{-1} Bismuth in 2% HNO_3 solution was the internal standard. In 2% HNO_3, a series of silver nitrate dilutions containing 0, 0.1, 0.5, 1, 5, 10, 50, and 100 ng mL^{-1} silver were prepared as standard solutions. All solutions were measured three times by ICP-MS to provide a mean value.

TXM 3D Imaging of AgNPs in a Single Cell. Cells were seeded to a dish and treated with AgNPs as ICP-MS experiment. Then, the exposed cells were rinsed with PBS three times and fixed by a 75% cold ethanol solution for 30 min. Removing the ethanol solution, cells were stained with 0.1% phosphotungstic acid solution (dissolved in 1× PBS) for 2 min. After rinsing with PBS three times, cells were dehydrated in gradients of ethanol from 50%, 75%, 80%, 90%, 95%, to 100%. It took 10 min for a dehydration to get the cell suspension dispersed in 100% ethanol. Cell suspension was dropped on a mylar thin film (Dupont) and air-dried. Then, gold particles with a 2−5 μm size as a reference were labeled on surface of the dried interested cells before imaging. The size range of gold particles distinguishes them from AgNP-contained vesicles. For each group, at least three cells were observed and a representative one was used in this manuscript. During the data acquisition of TXM, it is almost impossible to keep a sample's wobbling within several tens of nanometers due to the mechanical precision of rotation stage and thermal expansion effect. For a better reconstruction, some additional gold particles were used as characteristic feature for alignment before performing 3D reconstruction.

Single cell image was performed under a synchrotron radiation transmission X-ray microscopy (TXM) on beamline 4W1A at BSRF. To realize Zernike phase contrast imaging at high spatial resolution of 60 nm, an objective zone plate with 40 nm outermost zone width and a phase ring were equipped at a fixed energy of 8 keV. The cell sample on the film was placed on a holder in the vacuum chamber where the atmospheric pressure was kept at *ca.* 1 Torr. The cell sample on the holder was rotated from −80° to 80°. A fixed X-ray CCD camera with the pixel size of 13.5 μm was used to capture a series of two-dimensional radiographs for the sample at each projection view. At first, the background images for each sample were collected for the data treatment. Raw images were acquired with exposure time of 30 s and scan interval of 0.5°; thus, it took about 3 h to measure one cell sample. After a raw data collection, the following steps included the background deduction, the alignment, and the preliminary reconstruction done based on three softwares of TXM Controller, TXM Reconstructor, and TXM 3Dviewer, respectively. Further detailed information about segments of intracellular particles or vesicles, the analysis of three-dimensional distribution, and 3D animation can be obtained using Avizo 7.0 software (FEI).

Characterization Interaction of Silver Chemical Forms. To study the chemical forms of silver during cell uptake and exocytosis, we prepared cell samples as ICP-MS experiment. Totally, 5×10^6 cells were centrifuged, rinsed three times with PBS, collected to be a cell pellet, lyophilized, and transferred to a sealed tube filled with nitrogen gas to protect from oxidation. Before XANES measurement, dried cell samples were pressed to be a flat and uniform pellet adhering to a tape (3M). XANES spectra of silver K-edge were mainly recorded on beamline BL-14W1 at Shanghai Synchrotron Radiation Facility (SSRF) in China. Parts of experiments were performed on PF-AR NW10A at Photon Factory of High Energy Accelerator Research Organization (KEK), Japan. The transmission mode was used to measure XANES spectra for references (Ag foil, Ag_2S, Ag_2O, AgCl, $AgNO_3$ from Sigma) and the AgNPs suspension (10%, w/w). Equipped with a 32 element germanium solid-state detector, the fluorescence mode was adopted to collect XANES spectra for AgNP-exposed cells.

XANES data were first normalized in order to facilitate comparison of spectra from the varied samples, modes, or facilities. The preprocessed data were then analyzed with least-squares fitting (LSF) to calculate the ratio of silver species using IFEFFIT Athena software (CARS, the Consortium for Advanced Radiation Sources at University of Chicago).

Studying Interaction of MTs with Silver Ions. To confirm MT protein as one intracellular target proteins for silver ions, we used silver L_3-edge XANES on 4B7A beamline at BSRF. Atmospheric oxygen gas prefers to oxidize protein (such as MT) and cysteines that in the solution possibly disturb interactions of proteins and cysteines with Ag^+ ions. To avoid this problem, we thus studied the dynamic interaction process between Ag^+ ions and biological molecules in an inert gas (N_2). This beamline equipped with a chamber to fill with an inert gas is helpful to measure silver L_3-edge XANES. Total electron yield mode was used to measure the chemical forms of silver in reference compounds such as silver citrate and Ag_2S, which contain two forms such as Ag−OOC− (with carboxyl group) and Ag−S−, respectively. Fluorescence mode was adopted to characterize the silver chemical forms during the interaction of silver ions with MT. A 0.1 M $AgNO_3$ solution as silver ion form is measured. Ag−cysteine is prepared with 0.1 M Ag^+ and 0.1 M cysteine for 30 min in chloride-free PBS. About 0.1 M $AgNO_3$ solution was mixed with 0.5 mM MT (as the low dose) and 2 mM MT (as the high dose) for 30 min in chloride-free PBS at room temperature, respectively. Then, the liquid mixtures sealed in a thin plastic container were used to measure silver XANES spectra. Finally, after silver ions incubate with MT, the ratio of silver species based on Ag L_3-edge XANES was calculated using the same procedure above.

The *R* factor is used to judge the quality for the fitting data and the formula is

$$R \text{ factor} = \text{Sum}((\text{data-fitting data})^2)/\text{Sum}(\text{data}^2)$$

where the sums are over the data points in the fitting region. A value of *R* factor close to zero is regarded as a good quality.

The *R* factor values of all fitted data in Table 1, in Figures 6B and 7D are below 0.05, which means a good fitting data.

Furthermore, we used circular dichroism (CD) spectra to characterize the binding of silver ions to MTs by studying the changes in secondary structures of MT after their interaction. Before measurement, we incubated 200 μg mL^{-1} MT with silver ions (12.5, 25, and 50 μg mL^{-1}) in chloride-free PBS at 37 °C for 30 min. As prepared mixtures and 200 μg mL^{-1} MT in chloride-free PBS were used to measure the secondary structures of MT by Circular Dichroism (JASCO, J-810). The CD spectra were collected from the UV region between 190 and 300 nm. The α-helix has a positive peak at 192 nm and two negative peaks at 208 and 222 nm as the characteristics and the β-sheet has a negative band at 218 nm. The data were presented as mean residue ellipticity (deg cm^2 dmol^{-1}), and ratios of different types of secondary structures were also shown in Table 2.

Conflict of Interest: The authors declare no competing financial interest.

Acknowledgment. This work was financially supported by MOST 973 program (2011CB933400), the International Science & Technology Cooperation Program of China (2013DFG32340 and 2014DFG52500), the NSFC (21320102003, 21277037, 11205166, 11435002), the National Science Fund for Distinguished Young Scholars (11425520), the Major Equipment Program (2011YQ030134), and Beijing NSF (2152037). A part of the work was performed under the BSRF in Beijing, the SSRF in Shanghai, and the Photon Factory in KEK, Japan. We appreciated Prof. Peiping Zhu, Prof. Yidong Zhao, Dr. Lei Zheng, and Dr. Chengyan Ma at BSRF, Prof. Yuying Huang, Dr. Zheng Jiang, and Dr. Lihua Wang at SSRF for their supports in SR experiments.

Supporting Information Available: SR-TXM imaging theory and the tables about X-ray refraction index for different elements, characterization result of AgNPs, TEM image for untreated THP-1 cell, the modulation of mRNA levels by AgNPs or Ag^+ ions, the phase contrast SR-TXM images of AgNPs in a single cell, and TXM 3D images of AgNPs ,with 11 movies (avi files). This part also provided experimental methods like the assessment of LMPs, MMPs, and ROS, quantitative RT-PCR, and Western blot. The Supporting Information is available free of charge on the ACS Publications website at DOI: 10.1021/acsnano.5b02483.

REFERENCES AND NOTES

1. Krug, H. F. Nanosafety Research-Are We on the Right Track? *Angew. Chem., Int. Ed.* **2014**, *53*, 12304–12319.
2. Zhao, F.; Meng, H.; Yan, L.; Wang, B.; Zhao, Y. L. Nanosurface Chemistry and Dose Govern the Bioaccumulation and Toxicity of Carbon Nanotubes, Metal Nanomaterials and Quantum Dots *in Vivo*. *Sci. Bull.* **2015**, *60*, 3–20.
3. Chernousova, S.; Epple, M. Silver as Antibacterial Agent: Ion, Nanoparticle, and Metal. *Angew. Chem., Int. Ed.* **2013**, *52*, 1636–1653.
4. Xiu, Z. M.; Zhang, Q. B.; Puppala, H. L.; Colvin, V. L.; Alvarez, P. J. J. Negligible Particle-Specific Antibacterial Activity of Silver Nanoparticles. *Nano Lett.* **2012**, *12*, 4271–4275.
5. Chen, G. C.; Tian, F.; Zhang, Y.; Zhang, Y. J.; Li, C. Y.; Wang, Q. B. Tracking of Transplanted Human Mesenchymal Stem Cells in Living Mice Using Near-Infrared Ag_2S Quantum Dots. *Adv. Funct. Mater.* **2014**, *24*, 2481–2488.
6. De Jong, W. H.; Van Der Ven, L. T. M.; Sleijffers, A.; Park, M. V. D. Z.; Jansen, E. H. J. M.; Van Loveren, H.; Vandebriel, R. J. Systemic and Immunotoxicity of Silver Nanoparticles in an Intravenous 28 Days Repeated Dose Toxicity Study in Rats. *Biomaterials* **2013**, *34*, 8333–8343.
7. van der Zande, M.; Vandebriel, R. J.; Van Doren, E.; Kramer, E.; Herrera Rivera, Z.; Serrano-Rojero, C. S.; Gremmer, E. R.; Mast, J.; Peters, R. J. B.; Hollman, P. C. H.; et al. Distribution, Elimination, and Toxicity of Silver Nanoparticles and Silver Ions in Rats after 28-Day Oral Exposure. *ACS Nano* **2012**, *6*, 7427–7442.
8. George, S.; Lin, S. J.; Jo, Z. X.; Thomas, C. R.; Li, L. J.; Mecklenburg, M.; Meng, H.; Wang, X.; Zhang, H. Y.; Xia, T.; et al. Surface Defects on Plate-Shaped Silver Nanoparticles Contribute to Its Hazard Potential in a Fish Gill Cell Line and Zebrafish Embryos. *ACS Nano* **2012**, *6*, 3745–3759.
9. Li, L.; Sun, J.; Li, X. R.; Zhang, Y.; Wang, Z. X.; Wang, C. R.; Dai, J. W.; Wang, Q. B. Controllable Synthesis of Monodispersed Silver Nanoparticles as Standards for Quantitative Assessment of Their Cytotoxicity. *Biomaterials* **2012**, *33*, 1714–1721.
10. Singh, R. P.; Ramarao, P. Cellular Uptake, Intracellular Trafficking and Cytotoxicity of Silver Nanoparticles. *Toxicol. Lett.* **2012**, *213*, 249–259.
11. Foldbjerg, R.; Olesen, P.; Hougaard, M.; Dang, D. A.; Hoffmann, H. J.; Autrup, H. PVP-Coated Silver Nanoparticles and Silver Ions Induce Reactive Oxygen Species, Apoptosis and Necrosis in THP-1 Monocytes. *Toxicol. Lett.* **2009**, *190*, 156–162.
12. Hamilton, R. F.; Buckingham, S.; Holian, A. The Effect of Size on Ag Nanosphere Toxicity in Macrophage Cell Models and Lung Epithelial Cell Lines Is Dependent on Particle Dissolution. *Int. J. Mol. Sci.* **2014**, *15*, 6815–6830.
13. Yang, E. J.; Kim, S.; Kim, J. S.; Choi, I. H. Inflammasome Formation and IL-1β Release by Human Blood Monocytes in Response to Silver Nanoparticles. *Biomaterials* **2012**, *33*, 6858–6867.
14. Wang, H. Y.; Wu, L. X.; Reinhard, B. M. Scavenger Receptor Mediated Endocytosis of Silver Nanoparticles into J774A.1 Macrophages Is Heterogeneous. *ACS Nano* **2012**, *6*, 7122–7132.
15. Zhu, M. T.; Wang, B.; Wang, Y.; Yuan, L.; Wang, H. J.; Wang, M.; Ouyang, H.; Chai, Z. F.; Feng, W. Y.; Zhao, Y. L. Endothelial Dysfunction and Inflammation Induced by Iron Oxide Nanoparticle Exposure: Risk Factors for Early Atherosclerosis. *Toxicol. Lett.* **2011**, *203*, 162–171.
16. Chen, Z.; Meng, H.; Xing, G. M.; Yuan, H.; Zhao, F.; Liu, R.; Chang, X. L.; Gao, X. Y.; Wang, T. C.; Jia, G.; et al. Age-Related Differences in Pulmonary and Cardiovascular Responses to SiO_2 Nanoparticle Inhalation: Nanotoxicity Has Susceptible Population. *Environ. Sci. Technol.* **2008**, *42*, 8985–8992.
17. Wang, X.; Ji, Z. X.; Chang, C. H.; Zhang, H. Y.; Wang, M. Y.; Liao, Y. P.; Lin, S. J.; Meng, H.; Li, R. B.; Sun, B. B.; et al. Use of Coated Silver Nanoparticles to Understand the Relationship of Particle Dissolution and Bioavailability to Cell and Lung Toxicological Potential. *Small* **2014**, *10*, 385–398.
18. Zolnik, B. S.; Gonzalez-Fernandez, A.; Sadrieh, N.; Dobrovolskaia, M. A. Minireview: Nanoparticles and the Immune System. *Endocrinology* **2010**, *151*, 458–465.
19. Lim, D. H.; Jang, J.; Kim, S.; Kang, T.; Lee, K.; Choi, I. H. The Effects of Sub-Lethal Concentrations of Silver Nanoparticles on Inflammatory and Stress Genes in Human Macrophages Using cDNA Microarray Analysis. *Biomaterials* **2012**, *33*, 4690–4699.
20. Braakhuis, H. M.; Gosens, I.; Krystek, P.; Boere, J. A. F.; Cassee, F. R.; Fokkens, P. H. B.; Post, J. A.; van Loveren, H.; Park, M. V. D. Z. Particle Size Dependent Deposition and Pulmonary Inflammation after Short-Term Inhalation of Silver Nanoparticles. *Part. Fibre Toxicol.* **2014**, *11*, 49.
21. Liu, W.; Wu, Y.; Wang, C.; Li, H. C.; Wang, T.; Liao, C. Y.; Cui, L.; Zhou, Q. F.; Yan, B.; Jiang, G. B. Impact of Silver Nanoparticles on Human Cells: Effect of Particle Size. *Nanotoxicology* **2010**, *4*, 319–330.
22. Jiang, X. M.; Foldbjerg, R.; Miclaus, T.; Wang, L. M.; Singh, R.; Hayashi, Y.; Sutherland, D.; Chen, C. Y.; Autrup, H.; Beer, C. Multi-Platform Genotoxicity Analysis of Silver Nanoparticles in the Model Cell Line CHO-K1. *Toxicol. Lett.* **2013**, *222*, 55–63.
23. Kawata, K.; Osawa, M.; Okabe, S. *In Vitro* Toxicity of Silver Nanoparticles at Noncytotoxic Doses to HepG2 Human Hepatoma Cells. *Environ. Sci. Technol.* **2009**, *43*, 6046–6051.
24. Levard, C.; Hotze, E. M.; Lowry, G. V.; Gordon E. Brown, J. Environmental Transformations of Silver Nanoparticles: Impact on Stability and Toxicity. *Environ. Sci. Technol.* **2012**, *46*, 6900–6914.

25. Jiang, X. M.; Miclaus, T.; Wang, L. M.; Foldbjerg, R.; Sutherland, D. S.; Autrup, H.; Chen, C. Y.; Beer, C. Fast Intracellular Dissolution and Persistent Cellular Uptake of Silver Nanoparticles in CHO-K1 Cells: Implication for Cytotoxicity. *Nanotoxicology* **2015**, *9*, 181–189.
26. Shrivastava, R.; Kushwaha, P.; Bhutia, Y. C.; Flora, S. Oxidative Stress Induced Following Exposure to Silver and Gold Nanoparticles in Mice. *Toxicol. Ind. Health* **2014**, 10.1177/0748233714562623.
27. Starnes, D. L.; Unrine, J. M.; Starnes, C. P.; Collin, B. E.; Oostveen, E. K.; Ma, R.; Lowry, G. V.; Bertsch, P. M.; Tsyusko, O. V. Impact of Sulfidation on the Bioavailability and Toxicity of Silver Nanoparticles to *Caenorhabditis elegans*. *Environ. Pollut.* **2015**, *196*, 239–246.
28. Khan, F. R.; Paul, K. B.; Dybowska, A. D.; Valsami-Jones, E.; Lead, J. R.; Stone, V.; Fernandes, T. F. Accumulation Dynamics and Acute Toxicity of Silver Nanoparticles to *Daphnia magna* and *Lumbriculus variegatus*: Implications for Metal Modelling Approaches. *Environ. Sci. Technol.* **2015**, *49*, 4389–4397.
29. Liu, J. Y.; Hurt, R. H. Ion Release Kinetics and Particle Persistence in Aqueous Nano-Silver Colloids. *Environ. Sci. Technol.* **2010**, *44*, 2169–2175.
30. Shen, M. H.; Zhou, X. X.; Yang, X. Y.; Chao, J. B.; Liu, R.; Liu, J. F. Exposure Medium: Key in Identifying Free Ag^{+} as the Exclusive Species of Silver Nanoparticles with Acute Toxicity to *Daphnia magna*. *Sci. Rep.* **2015**, *5*, No. 967410.1038/srep09674.
31. Peretyazhko, T. S.; Zhang, Q.; Colvin, V. L. Size-Controlled Dissolution of Silver Nanoparticles at Neutral and Acidic pH Conditions: Kinetics and Size Changes. *Environ. Sci. Technol.* **2014**, *48*, 11954–11961.
32. Pratsinis, A.; Hervella, P.; Leroux, J. C.; Pratsinis, S. E.; Sotiriou, G. A. Toxicity of Silver Nanoparticles in Macrophages. *Small* **2013**, *9*, 2576–2584.
33. Kittler, S.; Greulich, C.; Diendorf, J.; Köller, M.; Epple, M. Toxicity of Silver Nanoparticles Increases During Storage Because of Slow Dissolution under Release of Silver Ions. *Chem. Mater.* **2010**, *22*, 4548–4554.
34. Pillai, S.; Behra, R.; Nestler, H.; Suter, M. J. F.; Sigg, L.; Schirmer, K. Linking Toxicity and Adaptive Responses Across the Transcriptome, Proteome, and Phenotype of *Chlamydomonas reinhardtii* Exposed to Silver. *Proc. Natl. Acad. Sci. U.S.A.* **2014**, *111*, 3490–3495.
35. Liu, J. Y.; Sonshine, D. A.; Shervani, S.; Hurt, R. H. Controlled Release of Biologically Active Silver from Nanosilver Surfaces. *ACS Nano* **2010**, *4*, 6903–6913.
36. Thalmann, B.; Voegelin, A.; Sinnet, B.; Morgenroth, E.; Kaegi, R. Sulfidation Kinetics of Silver Nanoparticles Reacted with Metal Sulfides. *Environ. Sci. Technol.* **2014**, *48*, 4885–4892.
37. Setyawati, M. I.; Yuan, X.; Xie, J. P.; Leong, D. T. The Influence of Lysosomal Stability of Silver Nanomaterials on Their Toxicity to Human Cells. *Biomaterials* **2014**, *35*, 6707–6715.
38. Eckhardt, S.; Brunetto, P. S.; Gagnon, J.; Priebe, M.; Giese, B.; Fromm, K. M. Nanobio Silver: Its Interactions with Peptides and Bacteria, and Its Uses in Medicine. *Chem. Rev.* **2013**, *113*, 4708–4754.
39. Leo, B. F.; Chen, S.; Kyo, Y.; Herpoldt, K. L.; Terrill, N. J.; Dunlop, I. E.; McPhail, D. S.; Shaffer, M. S.; Schwander, S.; Gow, A. The Stability of Silver Nanoparticles in a Model of Pulmonary Surfactant. *Environ. Sci. Technol.* **2013**, *47*, 11232–11240.
40. Chen, S.; Theodorou, I. G.; Goode, A. E.; Gow, A.; Schwander, S.; Zhang, J.; Chung, K. F.; Tetley, T. D.; Shaffer, M. S.; Ryan, M. P.; et al. High-Resolution Analytical Electron Microscopy Reveals Cell Culture Media-Induced Changes to the Chemistry of Silver Nanowires. *Environ. Sci. Technol.* **2013**, *47*, 13813–13821.
41. Levard, C.; Hotze, E. M.; Colman, B. P.; Dale, A. L.; Truong, L.; Yang, X. Y.; Bone, A. J.; Brown, G. E.; Tanguay, R. L.; Di Giulio, R. T.; et al. Sulfidation of Silver Nanoparticles: Natural Antidote to Their Toxicity. *Environ. Sci. Technol.* **2013**, *47*, 13440–13448.
42. Drescher, D.; Zeise, I.; Traub, H.; Guttmann, P.; Seifert, S.; Büchner, T.; Jakubowski, N.; Schneider, G.; Kneipp, J. *In Situ* Characterization of SiO_2 Nanoparticle Biointeractions Using Brightsilica. *Adv. Funct. Mater.* **2014**, *24*, 3765–3775.
43. Drescher, D.; Guttmann, P.; Buchner, T.; Werner, S.; Laube, G.; Hornemann, A.; Tarek, B.; Schneider, G.; Kneipp, J. Specific Biomolecule Corona Is Associated with Ring-Shaped Organization of Silver Nanoparticles in Cells. *Nanoscale* **2013**, *5*, 9193–9198.
44. Drescher, D.; Giesen, C.; Traub, H.; Panne, U.; Kneipp, J.; Jakubowski, N. Quantitative Imaging of Gold and Silver Nanoparticles in Single Eukaryotic Cells by Laser Ablation ICP-MS. *Anal. Chem.* **2012**, *84*, 9684–9688.
45. Greulich, C.; Diendorf, J.; Simon, T.; Eggeler, G.; Epple, M.; Köller, M. Uptake and Intracellular Distribution of Silver Nanoparticles in Human Mesenchymal Stem Cells. *Acta Biomater.* **2011**, *7*, 347–354.
46. Yu, S. J.; Chao, J. B.; Sun, J.; Yin, Y. G.; Liu, J. F.; Jiang, G. B. Quantification of the Uptake of Silver Nanoparticles and Ions to HepG2 Cells. *Environ. Sci. Technol.* **2013**, *47*, 3268–3274.
47. Hartmann, G.; Baumgartner, T.; Schuster, M. Influence of Particle Coating and Matrix Constituents on the Cloud Point Extraction Efficiency of Silver Nanoparticles (Ag-NPs) and Application for Monitoring the Formation of Ag-NPs from Ag^{+}. *Anal. Chem.* **2014**, *86*, 790–796.
48. Liu, J. Y.; Pennell, K. G.; Hurt, R. H. Kinetics and Mechanisms of Nanosilver Oxysulfidation. *Environ. Sci. Technol.* **2011**, *45*, 7345–7353.
49. Matassa, R.; Fratoddi, I.; Rossi, M.; Battocchio, C.; Caminiti, R.; Russo, M. V. Two-Dimensional Networks of Ag Nanoparticles Bridged by Organometallic Ligand. *J. Phys. Chem. C* **2012**, *116*, 15795–15800.
50. El Badawy, A. M.; Silva, R. G.; Morris, B.; Scheckel, K. G.; Suidan, M. T.; Tolaymat, T. M. Surface Charge-Dependent Toxicity of Silver Nanoparticles. *Environ. Sci. Technol.* **2011**, *45*, 283–287.
51. Chatterjee, A.; Santra, M.; Won, N.; Kim, S.; Kim, J. K.; Kim, S. B.; Ahn, K. H. Selective Fluorogenic and Chromogenic Probe for Detection of Silver Ions and Silver Nanoparticles in Aqueous Media. *J. Am. Chem. Soc.* **2009**, *131*, 2040–2041.
52. Chen, Y. T.; Chen, T. Y.; Yi, J.; Chu, Y. S.; Lee, W. K.; Wang, C. L.; Kempson, I. M.; Hwu, Y.; Gajdosik, V.; Margaritondo, G. Hard X-ray Zernike Microscopy Reaches 30 nm Resolution. *Opt. Lett.* **2011**, *36*, 1269–1271.
53. Yuan, Q. X.; Zhang, K.; Hong, Y. L.; Huang, W. X.; Gao, K.; Wang, Z. L.; Zhu, P. P.; Gelb, J.; Tkachuk, A.; Hornberger, B.; et al. A 30 nm-Resolution Hard X-ray Microscope with X-ray Fluorescence Mapping Capability at BSRF. *J. Synchrotron Radiat.* **2012**, *19*, 1021–1028.
54. Sakdinawat, A.; Attwood, D. Nanoscale X-ray Imaging. *Nat. Photonics* **2010**, *4*, 840–848.
55. Chen, C. Y.; Li, Y. F.; Qu, Y.; Chai, Z. F.; Zhao, Y. L. Advanced Nuclear Analytical and Related Techniques for the Growing Challenges in Nanotoxicology. *Chem. Soc. Rev.* **2013**, *42*, 8266–8303.
56. He, W. W.; Zhou, Y. T.; Wamer, W. G.; Boudreau, M. D.; Yin, J. J. Mechanisms of the pH Dependent Generation of Hydroxyl Radicals and Oxygen Induced by Ag Nanoparticles. *Biomaterials* **2012**, *33*, 7547–7555.
57. Levard, C.; Reinsch, B. C.; Michel, F. M.; Oumahi, C.; Lowry, G. V.; Brown, G. E. Sulfidation Processes of PVP-Coated Silver Nanoparticles in Aqueous Solution: Impact on Dissolution Rate. *Environ. Sci. Technol.* **2011**, *45*, 5260–5266.
58. Levard, C.; Mitra, S.; Yang, T.; Jew, A. D.; Badireddy, A. R.; Lowry, G. V.; Brown, G. E. Effect of Chloride on the Dissolution Rate of Silver Nanoparticles and Toxicity to *E. coli*. *Environ. Sci. Technol.* **2013**, *47*, 5738–5745.
59. Wang, L. M.; Li, Y. F.; Zhou, L. J.; Liu, Y.; Meng, L.; Zhang, K.; Wu, X. C.; Zhang, L. L.; Li, B.; Chen, C. Y. Characterization of Gold Nanorods *in Vivo* by Integrated Analytical Techniques: Their Uptake, Retention, and Chemical Forms. *Anal. Bioanal. Chem.* **2010**, *396*, 1105–1114.

60. Wang, L. M.; Li, J. Y.; Pan, J.; Jiang, X. M.; Ji, Y. L.; Li, Y. F.; Qu, Y.; Zhao, Y. L.; Wu, X. C.; Chen, C. Y. Revealing the Binding Structure of the Protein Corona on Gold Nanorods Using Synchrotron Radiation-Based Techniques: Understanding the Reduced Damage in Cell Membranes. *J. Am. Chem. Soc.* **2013**, *135*, 17359–17368.
61. Foldbjerg, R.; Irving, E. S.; Hayashi, Y.; Sutherland, D. S.; Thorsen, K.; Autrup, H.; Beer, C. Global Gene Expression Profiling of Human Lung Epithelial Cells After Exposure to Nanosilver. *Toxicol. Sci.* **2012**, *130*, 145–157.
62. Luther, E. M.; Schmidt, M. M.; Diendorf, J.; Epple, M.; Dringen, R. Upregulation of Metallothioneins After Exposure of Cultured Primary Astrocytes to Silver Nanoparticles. *Neurochem. Res.* **2012**, *37*, 1639–1648.
63. Lowry, G. V.; Gregory, K. B.; Apte, S. C.; Lead, J. R. Transformations of Nanomaterials in the Environment. *Environ. Sci. Technol.* **2012**, *46*, 6893–6899.
64. Loza, K.; Diendorf, J.; Sengstock, C.; Ruiz-Gonzalez, L.; Gonzalez-Calbet, J. M.; Vallet-Regi; Köller, M.; Epple, M. The Dissolution and Biological Effects of Silver Nanoparticles in Biological Media. *J. Mater. Chem. B* **2014**, *2*, 1634–1643.
65. Zook, J. M.; Long, S. E.; Cleveland, D.; Geronimo, C. L. A.; MacCuspie, R. I. Measuring Silver Nanoparticle Dissolution in Complex Biological and Environmental Matrices Using UV-Visible Absorbance. *Anal. Bioanal. Chem.* **2011**, *401*, 1993–2002.
66. Rainville, L. C.; Carolan, D.; Varela, A. C.; Doyle, H.; Sheehan, D. Proteomic Evaluation of Citrate-Coated Silver Nanoparticles Toxicity in *Daphnia magna*. *Analyst* **2014**, *139*, 1678–1686.
67. Verano-Braga, T.; Miethling-Graff, R.; Wojdyla, K.; Rogowska-Wrzesinska, A.; Brewer, J. R.; Erdmann, H.; Kjeldsen, F. Insights into the Cellular Response Triggered by Silver Nanoparticles Using Quantitative Proteomics. *ACS Nano* **2014**, *8*, 2161–2175.
68. Howitt, J.; Putz, U.; Lackovic, J.; Doan, A.; Dorstyn, L.; Cheng, H.; Yang, B.; Chan-Ling, T.; Silke, J.; Kumar, S.; et al. Divalent Metal Transporter 1 (DMT1) Regulation by Ndfip1 Prevents Metal Toxicity in Human Neurons. *Proc. Natl. Acad. Sci. U.S.A.* **2009**, *106*, 15489–15494.
69. Gottesman, M. M.; Fojo, T.; Bates, S. E. Multidrug Resistance in Cancer: Role of ATP-Dependent Transporters. *Nat. Rev. Cancer* **2002**, *2*, 48–58.
70. Kagi, J. H.; Vasak, M.; Lerch, K.; Gilg, D. E.; Hunziker, P.; Bernhard, W. R.; Good, M. Structure of Mammalian Metallothionein. *Environ. Health Perspect.* **1984**, *54*, 93–103.
71. Jimenez-Lamana, J.; Laborda, F.; Bolea, E.; Abad-Alvaro, I.; Castillo, J. R.; Bianga, J.; He, M.; Bierla, K.; Mounicou, S.; Ouerdane, L.; et al. An Insight into Silver Nanoparticles Bioavailability in Rats. *Metallomics* **2014**, *6*, 2242–2249.
72. Kaewamatawong, T.; Banlunara, W.; Maneewattanapinyo, P.; Thammachareon, C.; Ekgasit, S. Acute and Subacute Pulmonary Toxicity Caused by a Single Intratracheal Instillation of Colloidal Silver Nanoparticles in Mice: Pathobiological Changes and Metallothionein Responses. *J. Environ. Pathol. Toxicol. Oncol.* **2014**, *33*, 59–68.
73. Klemm, A. R.; Young, D.; Lloyd, J. B. Effects of Polyethyleneimine on Endocytosis and Lysosome Stability. *Biochem. Pharmacol.* **1998**, *56*, 41–46.
74. Repnik, U.; Stoka, V.; Turk, V.; Turk, B. Lysosomes and Lysosomal Cathepsins in Cell Death. *Biochim. Biophys. Acta, Proteins Proteomics* **2012**, *1824*, 22–33.
75. Ly, J.; Grubb, D.; Lawen, A. The Mitochondrial Membrane Potential ($\Delta\psi$m) in Apoptosis; an Update. *Apoptosis* **2003**, *8*, 115–128.
76. Green, D. R.; Reed, J. C. Mitochondria and Apoptosis. *Science* **1998**, *281*, 1309–1311.
77. Yun, W.; Lai, B.; Cai, Z.; Maser, J.; Legnini, D.; Gluskin, E.; Chen, Z.; Krasnoperova, A.; Vladimirsky, Y.; Cerrina, F. Nanometer Focusing of Hard X Rays by Phase Zone Plates. *Rev. Sci. Instrum.* **1999**, *70*, 2238–2241.
78. Di Fabrizio, E.; Romanato, F.; Gentili, M.; Cabrini, S.; Kaulich, B.; Susini, J.; Barrett, R. High-Efficiency Multilevel Zone Plates for KeV X-rays. *Nature* **1999**, *401*, 895–898.
79. Le Gros, M. A.; McDermott, G.; Larabell, C. A. X-ray Tomography of Whole Cells. *Curr. Opin. Struct. Biol.* **2005**, *15*, 593–600.
80. Schneider, G.; Guttmann, P.; Heim, S.; Rehbein, S.; Mueller, F.; Nagashima, K.; Heymann, J. B.; Muller, W. G.; McNally, J. G. Three-Dimensional Cellular Ultrastructure Resolved by X-ray Microscopy. *Nat. Methods* **2010**, *7*, 985–987.
81. Yang, X. Y.; Gondikas, A. P.; Marinakos, S. M.; Auffan, M.; Liu, J.; Hsu-Kim, H.; Meyer, J. N. Mechanism of Silver Nanoparticle Toxicity Is Dependent on Dissolved Silver and Surface Coating in *Caenorhabditis elegans*. *Environ. Sci. Technol.* **2012**, *46*, 1119–1127.
82. Adams, J. M.; Cory, S. The Bcl-2 Protein Family: Arbiters of Cell Survival. *Science* **1998**, *281*, 1322–1326.
83. Brown, J. M.; Wouters, B. G. Apoptosis, P53, and Tumor Cell Sensitivity to Anticancer Agents. *Cancer Res.* **1999**, *59*, 1391–1399.
84. Johnson, T. M.; Yu, Z. X.; Ferrans, V. J.; Lowenstein, R. A.; Finkel, T. Reactive Oxygen Species Are Downstream Mediators of P53-Dependent Apoptosis. *Proc. Natl. Acad. Sci. U.S.A.* **1996**, *93*, 11848–11852.
85. Reed, J. C. Double Identity for Proteins of the Bcl-2 Family. *Nature* **1997**, *387*, 773–776.